

Molecular dynamics simulations of coherent optical photon emission from shock waves in crystals

Evan J. Reed,^{1,2,*} Marin Soljačić,² Richard Gee,¹ and J. D. Joannopoulos²

¹Lawrence Livermore National Laboratory, Livermore, California 94551, USA

²Center for Materials Science and Engineering and Research Laboratory of Electronics, Massachusetts Institute of Technology, Cambridge, Massachusetts 02139, USA

(Received 29 November 2006; published 16 May 2007)

We have previously predicted that coherent electromagnetic radiation in the 1–100 THz frequency range can be generated in crystalline polarizable materials when subject to a shock wave or solitonlike propagating excitation [E. J. Reed *et al.*, Phys. Rev. Lett. **96**, 013904 (2006)]. In this work, we present analysis and molecular dynamics simulations of shock waves in crystalline NaCl which expand upon this prediction. We demonstrate that the coherent polarization currents responsible for the effect are generated by a nonresonant, nonlinear effect that occurs at the shock front. We consider the effect of thermal noise and various shock pressures on the coherent polarization currents and find that the amplitude generally increases with increasing shock pressure and decreasing material temperature. Finally, we present calculations of the amplitude and distribution of emitted radiation showing that the radiation can be directed or undirected under various realistic conditions of the shape of the shock front.

DOI: [10.1103/PhysRevB.75.174302](https://doi.org/10.1103/PhysRevB.75.174302)

PACS number(s): 62.50.+p, 41.60.-m, 42.25.Kb

INTRODUCTION

In our previous work, we have predicted that weak coherent radiation in the 100 THz frequency regime can be emitted under some circumstances when a shock wave propagates through a polarizable crystal, such as NaCl.¹ The coherence of the emitted radiation comes from the spatial coherence of the crystalline lattice, i.e., perfect periodicity, and the constant propagation speed of the shock wave. The radiation is generated by an oscillating material polarization resulting from the synchronized nonresonant motion of large numbers of atoms induced in the nonequilibrium region at the front of a planar shock wave propagating through the crystalline lattice. We believe that the mechanism responsible for this type of emission is fundamentally distinct from existing sources of many-cycle temporally coherent optical radiation in this frequency regime, which include “traditional” lasers based on stimulated emission, free-electron lasers,² and phonon related mechanisms.³

The study of shock waves in condensed matter usually focuses on states of the shocked material nanoseconds or more behind the shock front, where it is often assumed that the material has reached a stable state which is in thermodynamic equilibrium. Experimental observations of material states behind the shock front often focus on this region due to limitations on the time scale resolution of the instruments. In this work, we focus on an observable signature of subpicosecond time scale dynamics in the region within several nanometers of the shock front itself, where a highly nonequilibrium region exists in which atoms can be endowed with spectral components of the velocity that are much higher than those of normal phonon oscillations. Although considerable progress on the study of short-time and length scale phenomena behind a shock front is being made (e.g., Refs. 4–6), experimental approaches to study this regime remain extremely challenging.

In our original work,¹ we have predicted that coherent light can be emitted from a shock front by performing mo-

lecular dynamics simulations of shock waves in NaCl crystals. In a related paper, we have performed finite-difference time-domain (FDTD) simulations of Maxwell’s equations for a shock propagating through a one-dimensional (1D) polarizable crystal.⁷ Molecular dynamics simulations provide a more accurate description of the shocked material than can be provided by the FDTD simulations, including a three-dimensional (3D) description, a thermal disordering, and a lattice deformation. In this work, we expand upon our previous work by performing molecular dynamics studies to determine the level of robustness of the effect under various experimental conditions. We study the variation of the effect with changes in material temperature and shock pressure. In Ref. 1, we found that the amplitude and distribution of emitted radiation are extremely sensitive to the rise time and shape of the shock front surface. In this work, we study the amplitude and distribution of emitted radiation as a function of the shape of the shock front through explicit calculations of the fields. We find that the emitted coherent radiation can potentially be spatially directed if the shock front surface (normal to the propagation direction) is sufficiently flat. Finally, we provide some physical intuition for the origin of the effect and a comparison to other related effects along with a discussion of prospects for experimental observation.

I. PHYSICAL INTUITION FOR THE ORIGIN OF THE COHERENT RADIATION

It is well known that shock waves can induce static polarizations in a variety of materials. This phenomenon was first experimentally observed in the 1960s by measuring the time dependence of the generated current in a shocked material.^{8,9} For some distance behind the planar shock front, materials are typically characterized by a state of increasing uniaxial stress, i.e., the spatial gradient in the shock propagation direction component of the stress is nonzero. Such a spatial stress gradient breaks any inversion symmetry of the

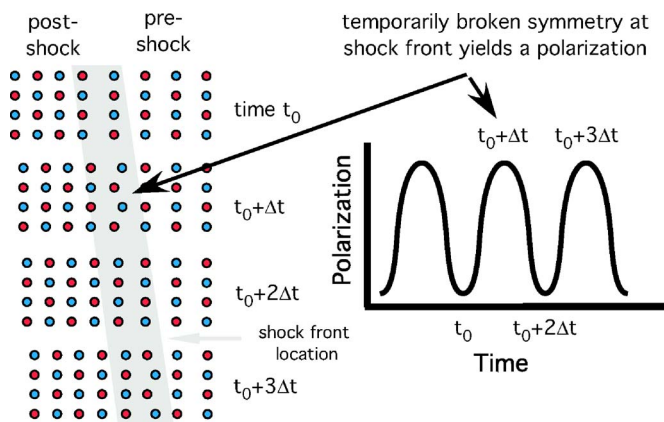


FIG. 1. (Color online) Schematic depicting a fashion in which a temporally periodic polarization can arise in a shocked polarizable crystal. Red and blue atoms on the left represent positively and negatively charged atoms. Atom positions within the shocked crystal are shown at four instances in time on the left with a gray area highlighting the shock front region. As the shock propagates over each lattice plane (left to right), the symmetry of atoms in that lattice plane can be temporarily broken yielding a nonzero static polarization of the atoms at the shock front. This process yields a temporally periodic polarization current which can potentially emit coherent radiation.

material by establishing a unique direction in the shocked material. The broken symmetry can lead to a static electric polarization along the shock propagation direction in any material, including isotropic liquids such as water.¹⁰

In this work, we consider a special case of shock-induced polarization that occurs only in crystalline materials when the shock front becomes very sharp, i.e., the shock front rise distance is a few lattice planes of the crystal or less. Figure 1 shows a schematic depicting a fashion in which a temporally periodic polarization can arise in a shocked polarizable crystal as a result of a thermal motion of the atoms. Red and blue atoms on the left represent positively and negatively charged atoms. Atom positions within the shocked crystal are shown at four instances in time on the left with a gray highlighting the shock front region. As the shock propagates over each lattice plane (left to right), the symmetry of atoms in that lattice plane can be temporarily broken yielding a nonzero static polarization of the atoms at the shock front. In Fig. 1, the static polarization points perpendicular to the plane of the shock wave. The broken symmetry can result from the atoms being different types with different masses or it can have other origins. In this schematic, the static polarization disappears in the material behind the shock front. A transient static polarization is produced each time the shock propagates through a lattice plane of the crystal. This process yields a temporally periodic polarization current which can potentially emit coherent radiation.

While the rise distance for the shock wave is about one lattice unit in length in the schematic in Fig. 1, the same general principle applies when the shock rise distance is more than one lattice unit, as is observed in the molecular dynamics simulations to be discussed in a subsequent section. In general, the shock wave produces some kind of ex-

citation of the atoms at the shock front, the precise details of which are not relevant to the degree of coherence but are relevant to the amplitude of the periodic polarization current. This excitation is temporally periodic in a crystal since a steady shock yields the same excitation to atoms in each periodic unit of the crystal. The temporally periodic nature of the excitation can potentially result in a temporally periodic polarization current if the excitation of the atoms yields a shift in net polarization for some period of time. A periodic polarization current can also potentially be produced if the shocked material (in the postshock region) possesses a net static polarization.

Of key importance to this effect are a high degree of crystalline order and a crystal consisting of charged or polarizable atoms or molecules that can couple to electromagnetic radiation, i.e., a polarizable crystal. It can also be seen from the schematic of Fig. 1 that the steepness of the shock front plays a role in determining the amplitude of the periodic component of the polarization current. A shock front spread out over many lattice planes may yield a smaller degree of overall broken symmetry resulting in smaller oscillations of static polarization and smaller oscillating polarization currents. The role of shock front thickness is studied in detail in Ref. 7.

For typical ionic crystal lattice constants (0.1–1 nm) and typical shock speeds in these materials (1–10 km/s), the coherent oscillation frequencies lie in the range from 1–100 THz, i.e., in the far-infrared and slightly below into the THz frequency regime. Such frequencies are well above the highest frequencies detectable in shock polarization current measurement experiments which utilize electronics to record signals. Optics-based techniques are typically used to detect signals in this frequency regime rather than electronics-based techniques.

II. ANALYTICAL THEORY

In this section, we use a 1D analytical approach to determine the possible frequencies of the polarization currents generated when a shock propagates along a high-symmetry direction in a polarizable crystal. From a macroscopic perspective, steady shock waves are characterized by self-similar waves, i.e., they have the property that they are invariant in a reference frame moving at the shock speed. This means that if the polarization of a continuum material is given by $\tilde{P}(x, t)$, then the polarization of the shock wave will be of the form $\tilde{P}(x - x', t - x'/v_s) = \tilde{P}(x, t)$ for any x' .

In this work, we are interested in the microscopic case where the material is not a continuum but instead consists of a periodic array of atomic lattice planes. The time-dependent polarization of the n th lattice plane in the shock propagation direction of the crystal can be represented by $P_n(t)$. Note that $P_n(t)$ includes thermal disordering effects since it is given by a sum over all atoms in lattice plane n . We consider a microscopic analog of the macroscopic steady state by considering the case where $P_{n-m}(t - m\frac{a}{v_s}) = P_n(t)$, where m is an integer and $P_n(t)$ represents the polarization components induced by the shock wave. Such a property represents a microscopi-

cally steady shock in a discrete lattice. This property of the polarization implies that $P_n(t)$ is of the form

$$P_n(t) = \sum_k e^{ik(na-v_s t)} \sum_\ell P'_{k,\ell} e^{-2\pi i \ell (v_s/a)t}, \quad (1)$$

where ℓ is an integer and k is a wave vector. For the frequencies considered in this work (above the phonon frequencies), the wavelength of any electromagnetic radiation generated by these polarization currents is orders of magnitude longer than the dimensions of the shock wave (tens of microns versus tens of nanometers, respectively). Therefore, the summation of polarization over all lattice planes in the shock wave will yield the frequency components that can be observed as emitted radiation. This will be discussed in greater detail in Sec. V. The polarization sum over all crystal lattice planes around the shock front is [i.e., the $k=0$ case of Eq. (1)]

$$\sum_n P_n(t) = \sum_\ell P'_{k,\ell} e^{-2\pi i \ell (v_s/a)t}. \quad (2)$$

The frequencies of these polarization oscillations are of the form

$$\omega = 2\pi \ell \frac{v_s}{a}. \quad (3)$$

These frequencies are integral multiples of the inverse time required for the shock to traverse a lattice unit of the crystal. As discussed in the previous section, the frequency $\frac{v_s}{a}$ is within the 1–100 THz range for typical shock speeds and lattice constants of ionic crystals. The discrete nature of these frequencies indicates that a significant degree of temporal coherence can be achieved if the shock speed and crystal lattice constants are fixed.

Equation (3) describes frequencies that are not phonon frequencies of the crystal. The frequencies of Eq. (3) are related to phonon frequencies of the crystal to the extent that the shock speed and lattice constant are also related to phonon frequencies, but any equivalence to a phonon frequency is coincidental. The difference between this effect and optical phonon excitation is discussed in detail in Sec. VI.

Equation (3) indicates that such frequencies can be produced by a shock wave propagating through a polarizable crystal but says nothing about the amplitude of such polarization oscillations. In the following section, we determine the amplitude of the polarization oscillations through a direct calculation.

III. MOLECULAR DYNAMICS SIMULATIONS: COHERENT POLARIZATION CURRENTS

In this section, we numerically explore the polarization currents generated by a shocked polarizable material by performing molecular dynamics simulations of shock waves propagating through crystalline NaCl. In a later section, we discuss in detail the connection between the polarization currents generated by the shock wave and the emitted radiation. Shock wave molecular dynamics simulations solve the classical equations of motion for atoms subject to an empirically constructed interaction potential and incorporate thermal ef-

fects and deformation of the crystal lattice. Such simulations are often referred to as nonequilibrium molecular dynamics simulations (NEMD) and are commonly employed to study shock waves in a variety of materials (see, for example, Refs. 11 and 12). In these calculations, planar shock waves are generated within 3D computational cells of perfectly crystalline atoms with cross section typically $17 \times 17 \text{ nm}^2$ and length in the shock propagation direction ranging from 158 to 235 nm [$(2-3) \times 10^6$ atoms] by constraining atoms at one edge of the long dimension of the computational cell to move into the cell like a planar piston (representing the mechanical driving force or object that generates the shock). Due to periodic boundary conditions in the directions transverse to the propagation direction, an infinitely planar shock propagates away from the constrained atoms into the cell which is oriented along either the [111] or [100] direction of NaCl. We have performed simulations with computational cell cross sections of up to $135 \times 135 \text{ nm}^2$ and obtained results in agreement with cross sections of $17 \times 17 \text{ nm}^2$ which indicates that the computational cell sizes are large enough that periodic boundary conditions do not play an artificial role in the behavior of the shocked material. We have utilized the LAMMPS molecular dynamics code.¹³

The molecular dynamics simulations were begun with NaCl in the rocksalt crystal structure. Atomic interactions were treated using unit charge Coulomb interactions with the following Lennard-Jones interactions: $\sigma_{\text{Na}^+-\text{Na}^+}=0.303 \text{ nm}$, $\sigma_{\text{Cl}^--\text{Cl}^-}=0.522 \text{ nm}$, $\sigma_{\text{Na}^+-\text{Cl}^-}=0.468 \text{ nm}$, $\epsilon_{\text{Na}^+-\text{Na}^+}=0.00225 \text{ eV}$, $\epsilon_{\text{Cl}^--\text{Cl}^-}=0.00268 \text{ eV}$, and $\epsilon_{\text{Na}^+-\text{Cl}^-}=0.00092513 \text{ eV}$. A 1 nm cutoff radius was utilized for the Lennard-Jones interactions. The full Coulomb potential is utilized with a particle-particle particle-mesh scheme for the long-range interactions. These potentials are found to yield a lattice constant (5.64 \AA) in agreement with the experimental value and to yield sound speeds that are higher than experimental measurements by 10%–20%. These empirical interatomic potentials are expected to provide a reasonably accurate material description when the crystal lattice is slightly compressed (a few percent) in the shock waves considered in this work.

Figure 2 shows the local material velocity as a function of position within the computational cell in the shock propagation direction for a typical shock simulation. A “piston” exists on the left side of the computational cell consisting of atoms with infinite mass fixed in the crystal structure, shown at the top of Fig. 2. The piston represents the source of the shock (e.g., a projectile from a gun in an experiment). Periodic boundary conditions exist in the computational cell in the direction transverse to the shock propagation direction yielding an infinitely planar shock wave propagating through a bulk material. The dimensions of the computational cell shown at the top of Fig. 2 are reduced from those employed in this work for clarity. At the start of the simulation in Fig. 2, the piston is given a velocity of 200 m/s to the right which drives a shock to the right into perfectly crystalline atoms at an initial temperature of 4.2 K. The shock front is characterized by a rapid transition between the material at rest and the material moving with the piston speed ($u_p=200 \text{ m/s}$ in this case). The shock front rise distance is about 1 nm or about three to four lattice planes. This steady-

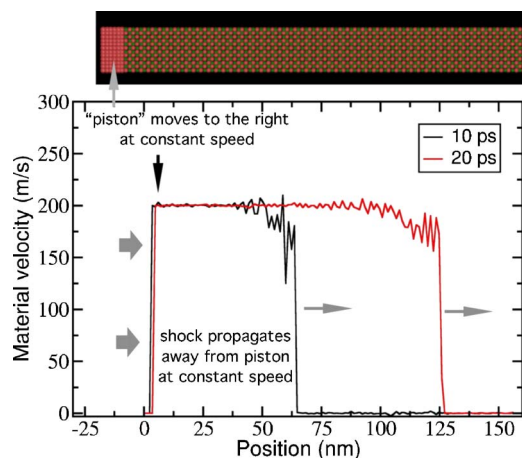


FIG. 2. (Color online) Material speed as a function of position in the shock propagation direction in a NaCl molecular dynamics simulation of a shock propagating in the [100] direction. A “piston” exists on the left side of the computational cell consisting of atoms with infinite mass fixed in the crystal structure (shown at top). The piston is given a velocity of 200 m/s to the right which drives a shock to the right. The dimensions of the computational cell shown at the top are reduced from those employed in this work for clarity.

state rise distance is rapidly reached in the early stages of the simulation and is consistent with the rapid rise observed in MD simulations of many other materials starting over a decade ago.¹⁴ The temperature difference between the shocked and unshocked materials is less than 1 K. The shock propagates until it reaches the opposite side of the computational cell, at which point the simulation ends.

Since each atom in the simulation possesses a charge, currents are generated by both the thermal motion of the atoms and the shock wave propagation. The shock propagation direction component of the total electric polarization current in the computational cell is $J = \sum_i v_{z,i} q_i$, where q_i is the charge and $v_{z,i}$ is the shock direction (z) component of the velocity of atom i . The polarization currents generated in the computational cell can be related to the electromagnetic emission. In this section, we focus purely on the polarization currents; the electromagnetic emission characteristics are discussed in detail in Sec. V.

Figure 3 shows the polarization current for approximately 30 ps duration simulations of shocks propagating in the [111] and [100] directions initiated with piston velocity of 200 m/s. This relatively small piston velocity generates a shock that applies a uniaxial strain of 0.03–0.04 to the post-shock material and increases the material temperature less than 1 K. Such strains are readily experimentally achievable using gun-driven projectile impacts (see, e.g., Ref. 15) and other approaches. Figure 3 compares the shocked and unshocked Fourier transforms of the shock propagation direction component of the total electric polarization current in the computational cell. Narrow peaks are observed in the shocked simulation that do not exist in the simulation with no shock. These peaks are the subject of this work.

The frequencies of the observed peaks agree well with the analysis of the previous section. Equation (3) predicts that polarization currents should occur in multiples of 5.4 THz in

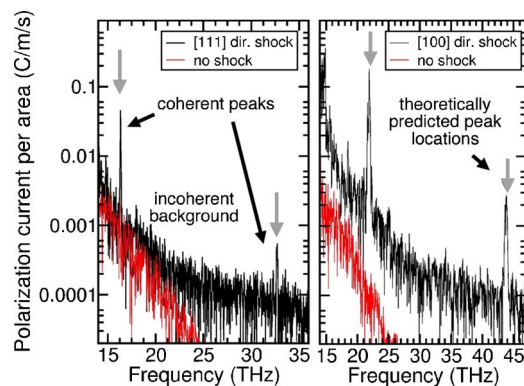


FIG. 3. (Color online) Fourier transform of the electric polarization surface current component in the shock propagation direction for molecular dynamics simulations of a shock propagating through NaCl in the [111] direction (left) and [100] direction (right). Narrow bandwidth, coherent peaks exist in the shocked simulations (black) that do not exist in the simulations without shocks. Gray arrows are emission frequencies predicted by Eq. (3). Thermal noise gives rise to an incoherent background.

the [111] case since the periodic unit for the [111] direction in NaCl $a=9.78 \text{ \AA}$ and the shock speed observed in the simulation is $v_s=5300 \text{ m/s}$. The 16 and 32 THz peaks on the left of Fig. 3 correspond to 3 and 6 times the fundamental frequency of 5.4 THz [i.e., $\ell=3$ and $\ell=6$ in Eq. (3)], in excellent agreement with theory (gray arrows). The 16 THz peak can be attributed to the structure within the unit cell of distance $a=3.26 \text{ \AA}$ [i.e., $\ell=1$ if $a=3.26$ in Eq. (3)], which is the distance between atomic lattice planes of like charge in the [111] direction (the NaCl crystal consists of alternating planes of positively and negatively charged atoms in the [111] direction). Lattice planes are compressed as the shock propagates through the crystal, generating an alternating polarization current with a frequency associated with the rate at which the shock propagates through the lattice planes. Equation (3) is also in good agreement with the [100] direction data, where $a=5.64 \text{ \AA}$ and the observed shock speed is $v_s=6200 \text{ m/s}$ with peaks corresponding to the $\ell=2$ and $\ell=4$ cases. The $\ell=2$ peak corresponds to the distance between neighboring lattice planes in the crystal (i.e., $\ell=1$ if $a=2.82 \text{ \AA}$).

If the shock speed is constant, the generated frequencies are constant and the coherence time of the emitted radiation is expected to be proportional to the time duration of the propagation of the shock wave. From the peak widths, the coherence time of the polarization current was determined to be about 17 ps (270 cycles) and 10 ps (220 cycles) for the 16 THz, [111] peak and 22 THz, [100] peak, respectively. For radiation emitted into vacuum, these coherence times correspond to coherence lengths of 5 and 3 mm, respectively. The coherence times are nearly Fourier transform limited (simulation durations are around 30 ps), suggesting that longer coherence lengths might be possible by increasing the shock propagation time and/or increasing crystal length. It is expected that the magnitude of fluctuations in the shock propagation speed will likely set the ultimate limit on the coherence time of the polarization currents.

Figure 4 shows the full spectrum of the [100] direction shock of Fig. 3. In addition to the narrow band peaks at

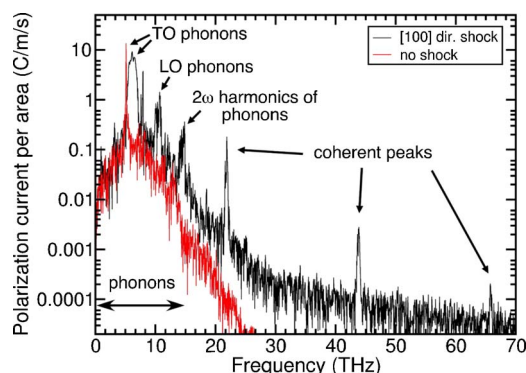


FIG. 4. (Color online) Electric polarization surface current component in the shock propagation direction for molecular dynamics simulations of a shock propagating through NaCl in the [100] direction with an initial temperature of 4.2 K. The shocked simulation (black) contains a number of excitations that are not present in the unshocked simulation (red). These include the longitudinal-optical (LO) phonons, harmonics of lower-frequency phonons, and the higher-frequency narrow band excitations discussed in this work. Transverse-optical (TO) phonons are also visible in both the shocked and unshocked simulations.

multiples of 22 THz, there are other peaks that arise at lower frequencies. Transverse-optical (TO) phonons are visible in both the shocked and unshocked simulations. The shocked simulation shows longitudinal-optical (LO) phonons and some nonlinear harmonics (around 16 THz) of lower-frequency phonons (around 8 THz). The TO and LO modes are ordinarily expected to produce a macroscopic polarization current, i.e., a polarization current that does not integrate to near zero over the whole computational cell. The highest linear phonon frequencies in this system are the LO phonons around 10–11 THz. Therefore, the peaks at 22 THz are not due to phononlike resonant excitations. They result from highly nonresonant nonlinear processes at the shock front. Observation of these peaks requires that there be spectral components of atom velocities at these higher frequencies around the shock front. Such high-frequency components of atomic motion can be generated only if the shock front (or part of it) is very sharp. The natural shock front rise distances in the molecular dynamics simulations are several lattice planes. To our knowledge, such an experimental measurement has never been made in the case of a wave characterized by purely elastic deformation of the crystal lattice. The mechanism presented here presents an enabling path toward making such a measurement.

Figure 4 shows that the $\ell=1$ peak of Eq. (3) corresponding to 11 THz falls within the LO phonons. Therefore, it is difficult to determine if the $\ell=1$ process occurs with any significant amplitude. However, the $\ell=3$ (33 THz) and higher odd multiple peaks are not observed. This suggests that polarization processes associated with the two lattice planes of the full lattice constant of the crystal in the [100] direction (i.e., odd and even ℓ) are much less significant than those associated with a single lattice plane of the crystal (i.e., only even ℓ). This result might be expected since the lattice planes are equivalent to within a translation within the plane of the shock.

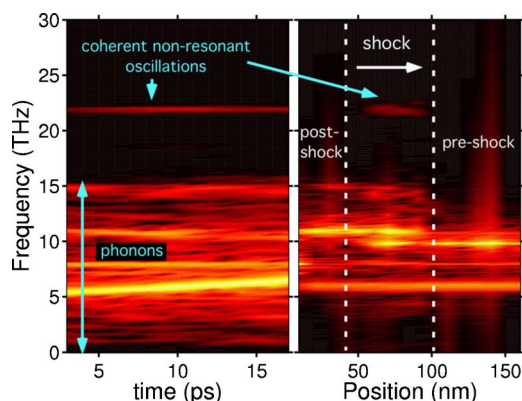


FIG. 5. (Color online) Electric polarization surface current component in the shock propagation direction for molecular dynamics simulations of a shock propagating through NaCl in the [100] direction with an initial temperature of 4.2 K. The left plot shows that the 22 THz signal (nonresonant) polarization current occurs for the duration of the shock propagation with roughly constant amplitude. On the right is a plot of frequency as a function of position in the computational cell in the shock propagation direction. During the time over which this Fourier transform is taken, the shock front propagates between the white dotted lines. This plot shows that the 22 THz current occurs in the region where the shock front is located rather than behind it or in front of it.

While there appear to be spectral components generated by the shock within the phonon frequencies, prediction of the magnitude of these peaks in the emitted electromagnetic radiation is complicated by several factors. The frequency regime around the TO and LO phonons is a regime in which phonon-photon interactions absorb and reflect radiation (polaritonic band gap) which may diminish or preclude observation of emitted spectral components. However, shock waves can be generated in very thin films with thicknesses of down to 10 nm and potentially less; it may be possible that absorption and reflection effects can be small enough in such systems to enable observation of emitted radiation in this frequency regime. The nonresonant excitations at 22 THz and above are far above the phonon frequencies where the material becomes transparent. Therefore, predictions of emitted radiation from these peaks are considerably simplified. This is discussed in more detail in Sec. V.

Figure 5 shows Fourier transforms of the electric polarization surface current component in the shock propagation direction for the simulation of Fig. 4. On the left is a plot of frequency as a function of time (the Fourier transform window length for each time on this plot is 5 ps). This plot shows that the 22 THz signal occurs for the duration of the shock propagation. The peaks below 16 THz are phonon related. On the right side of Fig. 5 is a plot of frequency as a function of position in the computational cell in the shock propagation direction. During the time window over which this Fourier transform is taken (from 5 to 15 ps), the shock front propagates between the white dotted lines. This plot shows that the polarization current at 22 THz occurs in the region where the shock front is located rather than behind it or in front of it, consistent with the schematic in Fig. 1. This indicates that the excitation is nonresonant and leaves no

excitation at 22 THz in the wake of the shock. Such behavior is expected since the highest (linear) phonon frequencies are far lower, around 11 THz. The transverse-optical phonon mode can be seen around 6 THz and the split between the pre- and postshock values of the LO phonon mode can be seen around 10–11 THz. The signal at 15 THz is observed behind the shock. This indicates that the excitation consists of Brillouin-zone center harmonics of lower-frequency phonon modes.

Since the polarization current responsible for the 22 THz peak exists only at the shock front, it might be expected that any phase transformations or plastic deformation of the material behind the shock front may not affect the coherent emission in a significant way other than to potentially change the shock speed with time. We find no evidence for atomic disordering of the crystal behind the shock wave for the relatively weak shock waves considered in the 200 m/s piston speed simulations. We have performed simulations with computational cell cross sections of up to $135 \times 135 \text{ nm}^2$ and obtained coherent polarization current results in agreement with computational cell cross sections of $17 \times 17 \text{ nm}^2$ which were employed for all of the figures in this work. This indicates that the computational cell sizes are large enough that periodic boundary conditions do not cause numerical artifacts in the behavior of the shocked material.

The discussion so far has focused on the polarization current component in the shock propagation direction. The components of the polarization current that are transverse to the shock propagation direction show only the TO phonon. This might be expected since, at least for relatively small piston speeds, the transverse components of motion of the atoms induced by the shock wave will be smaller than the components parallel to the propagation direction due to the initially longitudinal excitation process of the shock wave. However, Eq. (3) applies to the transverse component of the polarization current in addition to the longitudinal component; it is therefore possible that coherent polarization current components transverse to the shock propagation direction could be generated under some circumstances.

It is well known that the use of periodic boundary conditions with Coulomb interactions in molecular dynamics simulations can potentially yield numerical artifacts when the computational cell has a net dipole moment (see, e.g., Ref. 16). Since we are studying oscillations of the net polarization of the shocked material, we have performed a calculation in a “mirror image” computational cell configuration such that oscillations generated by the shock wave do not result in polarization oscillations of the whole computational cell. For a 200 m/s piston speed shock in the [100] direction, the nonresonant peaks (22 THz and above) are not significantly affected by the periodic boundary conditions, but some of the phonon frequencies and amplitudes are altered as might be expected.

The 200 m/s piston speed employed in these simulations is relatively small, generating material strains of only a few percent. The interatomic potentials utilized in the molecular dynamics simulations provide a reasonable description of NaCl (and a qualitative description of other rocksalt alkali halides) under conditions of low strain. However, substantially larger material strains can be readily generated in

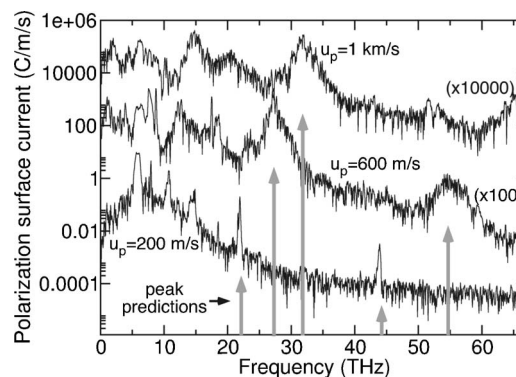


FIG. 6. Comparison of electric polarization surface current component in the shock propagation direction for molecular dynamics simulation shocks propagating through a NaCl model in the [100] direction with an initial temperature of 4.2 K. The shocks were generated using piston speeds of 200, 600, and 1000 m/s. The 600 and 1000 m/s curves are shifted up by factors of 100 and 10000, respectively. Gray arrows are emission frequencies predicted by Eq. (3). As the piston speeds increase, the peaks broaden (becoming less coherent) and increase in amplitude. The broadening is due in part to unsteady shock speeds.

shock wave experiments. Figure 6 shows simulations using larger piston velocities with the caveat that the intermolecular potentials may not necessarily be representative of NaCl under these more extreme conditions. The larger piston velocity simulations are expected to provide a qualitative picture of possible types of behavior for a shocked ionic crystal.

Figure 6 shows a comparison of the electric polarization surface current component in the shock propagation direction for shocks propagating in the [100] direction with an initial temperature of 4.2 K. The shocks were generated using piston speeds of 200, 600, and 1000 m/s. The 600 and 1000 m/s curves are multiplied by factors of 100 and 10 000, respectively, for clarity. The 200 m/s simulation data are also shown in Figs. 3 and 5. Gray arrows are emission frequencies predicted by Eq. (3). As the shock speeds increase, the peaks broaden (becoming less coherent) and increase in amplitude. The broadening effect at higher piston speeds is due in part to unsteady shock propagation speeds. When the shock speed is not constant, the emission frequencies will also not be constant, resulting in a broadened peak. The shock speed varies from 7700 to 7600 m/s in the 600 m/s piston speed case and 9300 to 8800 m/s in the 1000 m/s piston speed case. For higher piston speeds, the time required for vibrational relaxation behind the shock may be longer, resulting in unsteady shock speeds for a longer period of time and more time required for the shock to reach a steady speed. One could speculate that given the sufficient shock propagation time (i.e., longer crystal) for a steady shock speed to be reached, the width of the polarization peaks will become more narrow for higher piston speeds.

IV. THERMAL EFFECTS

It might be expected that thermal disordering of the crystal lattice could have an effect on the amplitude and degree

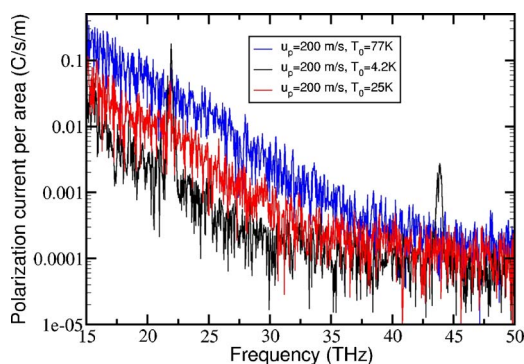


FIG. 7. (Color online) Electric polarization surface current component in the shock propagation direction for molecular dynamics simulations of a shock propagating through NaCl in the [100] direction with a piston speed of 200 m/s for various temperatures. The coherent peak amplitude at 22 THz decreases with increasing temperature and the background increases with increasing temperature.

of coherence of the generated polarization currents. In this section, we clarify this issue by performing molecular dynamics simulations at higher initial temperatures. Figure 7 is a comparison of the polarization currents generated in shocks in the [100] direction with 200 m/s piston speed for a range of initial temperatures. As the initial temperature of the material is increased, the amplitude of the coherent peak decreases and the incoherent background amplitude increases. The coherent peak is still visible at 25 K but not at 77 K.

The background amplitude increases with increasing temperature due to the increased thermal motion of the atoms. The decrease in amplitude of the lower-frequency coherent peak and extinction of the higher-frequency coherent peak require a more subtle explanation. As the material temperature changes, it is possible for the shock front rise time to change as well since the effective viscosity and other properties of the material may change. As discussed previously, the rise time of the shock is expected to play a role in the amplitude of the coherent peaks. Another source of peak amplitude variation with temperature may be the thermal disordering of the crystal lattice, i.e., it becomes less periodic as the temperature increases. An increase in thermal broadening of the atomic positions could potentially reduce the amplitude of the coherent peak.

Figure 7 indicates that the coherent peak is swamped by noise when the temperature increases to 77 K. However, the relative magnitudes of the coherent peak and the incoherent background are expected to scale differently with the size of the computational cell. The computational cell sizes and shock propagation times of our simulations are (necessarily) substantially smaller than the shock front areas and propagation times of experiments. We will now show that it may be possible for the coherent peaks to be observable above the thermal background at higher temperatures under experimental conditions that are beyond the capability of the simulations.

To estimate the scaling with computational cell size of the relative magnitudes of the coherent peak and the incoherent background, we use an Einstein model of the crystal. Within

this model, the polarization current per unit area in a particular direction within the computational cell at frequency ω is

$$j(\omega) = \frac{1}{\tau} \int_0^\tau dt \left(\sum_{j=0}^{N-1} \frac{a_j}{A} e^{i\omega_p t} + cn^{2/3} e^{i\omega_0 t} \right) e^{-i\omega t}, \quad (4)$$

where τ is the duration of the shock propagation (simulation duration), N is the number of atoms in the computational cell, ω_p is the Einstein phonon frequency, ω_0 is the frequency of the coherent portion of the current, c is the amplitude coefficient of the coherent portion of the current, A is the area of the computational cell perpendicular to the shock propagation direction (shock front area), n is the number density of atoms, and ω_0 is the coherent polarization current frequency. The amplitudes of the phonons a_j are taken to have random phases, i.e., $a_j \equiv \tilde{a} e^{i2\pi\phi_j}$, where ϕ_j is a random variable with $0 \leq \phi_j < 1$. The coherent portion of $j(\omega_0)$ is $cn^{2/3}$ and the expected magnitude of the incoherent portion scales like $\sim \frac{\tilde{a}}{A} \frac{\sqrt{N}}{\tau}$. In an NEMD shock wave simulation, the maximum shock propagation time is related to the size of the computational cell through the relation $\tau = V/(Av_s)$, where V is the computational cell volume. Combining these relations, the ratio of the amplitude of the coherent peak to the incoherent background scales like

$$\left| \frac{j_{\text{coherent}}(\omega_0)}{j_{\text{incoherent}}(\omega_0)} \right| \sim \frac{c}{\tilde{a}} \sqrt{V}. \quad (5)$$

Since the computational cell volume V is far smaller in magnitude in the simulations than for a typical shock wave experiment and far smaller than the wavelengths of radiation of interest, the incoherent noise background in the simulations is larger than would be expected in an experiment. This relation indicates that the ratio can be increased by increasing the volume of the computational cell.

Since the amplitude of the coherent polarization current can also be increased by increasing the shock amplitude, one might ask whether it is possible to observe the coherent signal above the background even at room temperature. Figure 8 shows a comparison of the electric polarization surface current component in the shock propagation direction for various piston speeds in molecular dynamics simulation shocks propagating through a NaCl model in the [100] direction with an initial temperature of 300 K. This plot is analogous to Fig. 6 but with a 300 K initial temperature. Coherent peaks are not observed above the noise background with a 200 m/s piston speed, but they are observed for higher piston speeds. In addition to changing the amplitude of the peaks, increasing the piston speed also increases the shock speed which increases the peak frequency. Gray arrows are emission frequencies predicted by Eq. (3).

Figure 9 compares the 1000 m/s piston speed simulations of Figs. 6 and 8 with initial temperatures of 4.2 and 300 K, respectively. The peak amplitude around 30 THz is lower at 300 K than in the 4.2 K case, but the bandwidth is substantially narrower in the 300 K case. The coherence length of the 300 K peak is about 180 cycles of the light, as given by the peak bandwidth. The narrowness of the 300 K peak compared to the 4.2 K peak is due to a more rapidly achieved steady shock speed at 300 K. At higher temperatures, the

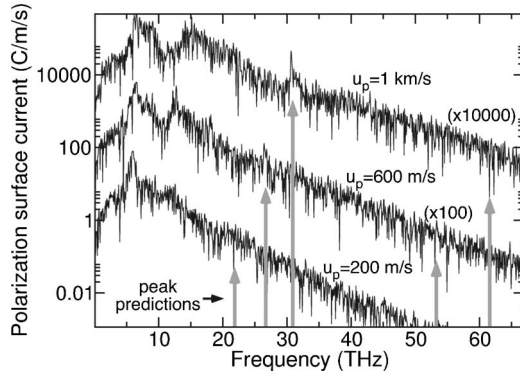


FIG. 8. Comparison of electric polarization surface current component in the shock propagation direction for shocks propagating through a NaCl in the [100] direction with an initial temperature of 300 K. The shocks were generated using piston speeds of 200, 600, and 1000 m/s. The 600 and 1000 m/s curves are multiplied by factors of 100 and 10 000, respectively, for clarity. This plot is equivalent to Fig. 6 but with a 300 K initial temperature. Gray arrows are emission frequencies predicted by Eq. (3). Coherent peaks are not observed with a 200 m/s piston speed, but they are observed for higher piston speeds.

vibrational equilibration time behind the shock wave occurs more quickly, allowing the shock to reach a steady speed more quickly than at lower temperatures.

Despite the increased thermal disorder of the crystalline lattice at 300 K, the coherence length of the polarization current is appreciable. Since the polarization current is a summation over many atoms, only the average locations of the atoms in a lattice plane are relevant. The thermally disordered average positions are still crystalline, giving rise to significant coherence lengths.

V. RADIATION EMISSION CHARACTERISTICS

The molecular dynamics simulations yield polarization currents but they do not explicitly solve Maxwell's equations

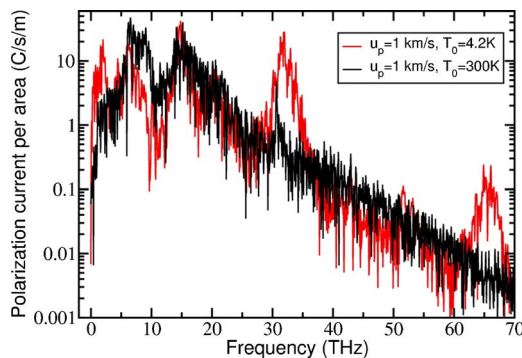


FIG. 9. (Color online) Comparison of Fourier transforms of the electric polarization surface current component in the shock propagation direction for shocks propagating through a NaCl model in the [100] direction with initial temperatures of 4.2 and 300 K. The shocks were generated using piston speeds of 1000 m/s. The peak height above the incoherent background is lower and the bandwidth is narrower in the 300 K case.

for the electric and magnetic fields that radiate away from the shock wave. However, since the wavelength of radiation emitted at frequencies considered here (longer than $10 \mu\text{m}$) is much longer than the dimensions of the computational cell, it is expected that the total polarization current generated in the computational cell will be closely related to the generated electromagnetic radiation for frequencies above the phonon frequencies (above about 10 THz in this NaCl model) where the material has good transmission properties. At lower frequencies, the relationship is complicated by absorption and polariton gaps. In this section, we focus on the determination of the electromagnetic emission for frequencies above the phonon frequencies where the material is transparent.

The molecular dynamics simulations enable simulation of experimentally relevant lengths of material in the shock propagation direction, but the area of shock fronts in typical experiments ($100 \times 100 \mu\text{m}^2$ to $1 \times 1 \text{cm}^2$) is much larger than can be simulated ($100 \times 100 \text{nm}^2$). The shock waves in the molecular dynamics simulations are planar, but deviations of the shock front from perfect planarity on these longer length scales are experimentally inevitable and we will show that such deviations can affect emission characteristics. The electric field emitted from a nonplanar shock front in the far-field limit, far from the shock front, can be calculated using polarization current magnitude data from the infinitely planar shock molecular dynamics simulations as an integral over polarization current at the shock front,

$$|E(\vec{r})|^2 = \left[\frac{\mu_0 \omega \sin(\theta)}{4\pi |r|} \right]^2 \left| \int_{\text{shock}} d\vec{r}' j(\vec{r}') e^{-i\omega(|\vec{r}-\vec{r}'|/c)} \right|^2, \quad (6)$$

where j is the ω frequency component of the polarization current on the shock front surface (oriented normal to the shock front) obtained from molecular dynamics simulations and θ is the angle between \vec{r} and a vector normal to the shock front. The integral is over the shock front, taken to be in the x - y plane. The polarization current is well described by $j(\vec{r}') = j_0 e^{i\omega[z(\vec{r}')/v_s]}$, where j_0 is the magnitude of the ω component of the polarization current obtained from MD simulations of planar shocks and $z(\vec{r}')$ describes the position of the shock front in the propagation direction as a function of location on the front surface \vec{r}' . The magnitude of j is constant everywhere on the shock front and only the phase is allowed to vary as a function of position on the shock front if the shock is not perfectly planar. The magnitude j_0 comes directly from molecular dynamics simulations of infinitely planar shock waves (the shock waves in the molecular dynamics simulations are infinitely planar due to periodic boundary conditions in the directions transverse to the computational cell). Transverse phase variations occur on length scales much larger than the size of the simulation computational cell.

The phase of j can be seen to depend very sensitively on the position of the shock front z to variations of a few angstroms in the case of NaCl ($2\pi \frac{v_s}{\omega}$ is on the order of angstroms). Figure 10 shows schematically how variations of the

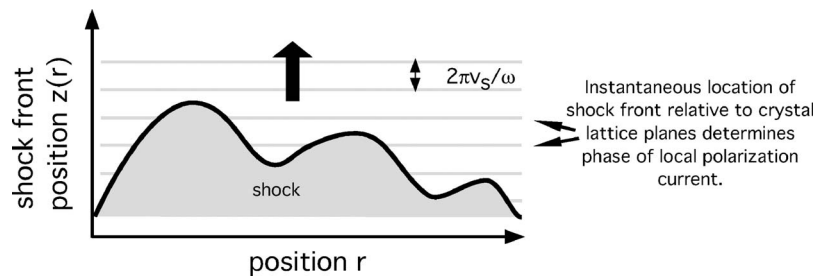


FIG. 10. Schematic depicting variations of shock front position $[z(r)]$ superimposed on periodic units of the crystal (e.g., lattice planes). The phase of the polarization current $j(\vec{r}') = j_0 e^{i\omega[z(\vec{r}')/v_s]}$ depends very sensitively on the flatness of the shock front on the length scale of $2\pi v_s/\omega$ which is 0.282 nm in the case of the 22 THz peak observed in NaCl shocked along the $[100]$ direction. Variations in phase across the surface of the shock front determine, in part, the emission characteristics through Eq. (6).

flatness of the shock front on the length scale of $2\pi \frac{v_s}{\omega}$ can determine the phase of the oscillating polarization current locally at a point on the shock. Therefore, the distribution and intensity of the emitted radiation (but not the coherence length) will depend very sensitively on the shape of the shock front. Note that this schematic description also applies when the shock front is spread out over many lattice planes. Using Eq. (6) and the polarization current from planar shock wave molecular dynamics simulations, the electromagnetic emission can be calculated for a given shock front shape, $z(r)$. Equation (6) can be thought of as a phase-matching condition between emitted radiation and the polarization current on the shock surface.

Since the precise atomic scale details of the shape of shock fronts vary under the variety of achievable experimental conditions, we consider several cases here to explore the range of possible emission characteristics. The first case we consider is that of an infinitely planar shock. In this case, no radiation will be emitted because the polarization of the polarization current is oriented normal to the plane of the shock wave. If the polarization currents were oriented within the plane of the shock, then this case would yield directed radiation propagating normal to the shock front plane.

The second case we consider is that of a perfectly planar shock front with significant subwavelength dimensions. In this case, the shock front can be treated as an oscillating dipole and the radiation characteristics are those associated with an oscillating dipole. The phase-matching issues mentioned above do not apply in this subwavelength example. In this case, the propagating shock wave acts as a point source of radiation emitting a dipolelike distribution of radiation (peaked in the plane of the shock wave) with power,

$$p(\omega) = \frac{\mu_0 \omega^2 j_0^2 A^2}{12\pi c}, \quad (7)$$

where j_0 is the polarization current per unit area on the shock front surface (plotted in Fig. 3) and A is the shock front area. For a 5 μm diameter shock front (e.g., a laser-driven shock) and $j_0 = 0.18 \text{ C/m s}$ for the 22 THz peak on the right side of Fig. 3, Eq. (7) predicts that the power coherently radiated at 22 THz is $3 \times 10^{-11} \text{ W}$ while the shock propagates. Collecting and focusing this radiation can yield electric-field amplitudes up to about 0.1 V/cm.

The third case we consider is that of an experimentally achievable shock front shape reported by Moore *et al.*, with a root-mean-square variation of 0.7 nm over a 75 μm area of the shock front.¹⁷ This shock was produced using a laser-drive technique. Based on this experimental capability, we consider a shock front shape of the form

$$z(r) = \alpha |r|^2, \quad (8)$$

with $\alpha = 0.45 \text{ m}^{-1}$ which provides a similar curvature to that experimentally observed in Ref. 17. We assume that the shock front is smooth apart from the curvature of Eq. (8). Figure 11 shows the spatial dependence of the electric-field magnitude computed from Eq. (6) for a $100 \times 100 \mu\text{m}^2$ shock front area using $j_0 = 0.18 \text{ C/m s}$ for the 22 THz peak from the 4.2 K NaCl $[100]$ planar molecular dynamics simulation with $u_p = 200 \text{ m/s}$ and $2\pi v_s/\omega = 0.282 \text{ nm}$. The shock front is located at the origin and the polarization (normal to the shock front plane) is in the vertical axis of the plot. Radiation is emitted in most directions except directly up and down (the shock propagation direction) due to the orientation of the polarization current direction. The emission appears approximately dipolelike in nature.

For a more planar shock front with less curvature, the radiation can be directed. Figure 12 shows how this can be accomplished. This figure was computed using

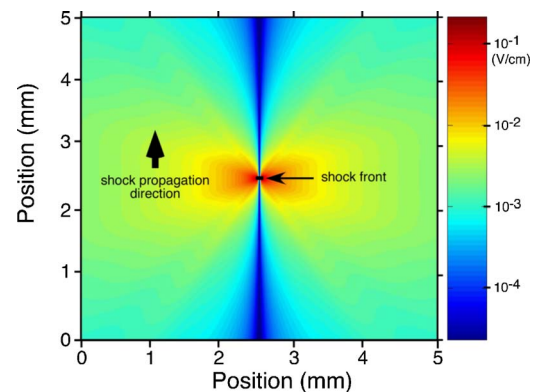


FIG. 11. (Color online) Electric-field magnitude at 22 THz from a $100 \times 100 \mu\text{m}^2$ square shock front for $j_0 = 0.18 \text{ C/m s}$ for the 22 THz peak on the right side of Fig. 3 and a curved shock front based on the experimentally observed shock front in Ref. 17.

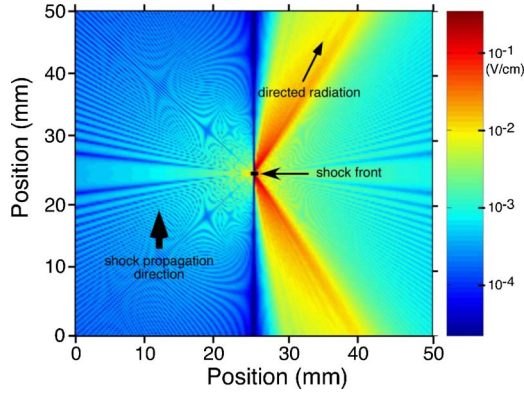


FIG. 12. (Color online) Electric-field magnitude at 22 THz from a $1 \times 1 \text{ mm}^2$ square shock front for $j_0=0.18 \text{ C/m s}$ for the 22 THz peak on the right side of Fig. 3 and a curved, tilted shock front. Emission of directed radiation can be achieved for this sufficiently planar shock wave.

$$z(r) = \alpha|r|^2 + \beta r_x, \quad (9)$$

with $\alpha=0.0045 \text{ m}^{-1}$ and $\beta=7 \times 10^{-6}$ for a square shock front of $1 \times 1 \text{ mm}$. The quantity r_x is the x component of the vector \vec{r} in the plane of the shock wave. This shock front shape is flatter than in Fig. 11 and includes a net tilt with respect to the crystal axis (the β term). The tilt angle is approximately 10^{-5} rad which is achievable using laser-driven shocks by tilting the drive beam incidence angle. Figure 12 shows how the radiation can be directed in this case. The tilt gives rise to a phase variation of the polarization current across the shock front that results in directed emission in a direction other than the shock propagation direction where the $\sin(\theta)$ term in Eq. (6) diminishes the radiation output.

In the limiting case of a perfectly flat shock front with some tilt, the shock emits a directed collimated beam. The electric-field magnitude in the beam is on the order of 0.1 V/cm for $j_0=0.18 \text{ C/m s}$ for the 22 THz peak on the right side of Fig. 3. For detection purposes, the collimated beam can be focused to enhance the electric-field amplitude, potentially by orders of magnitude. Use of a larger piston speed can also enhance j_0 leading to larger electric fields.

While a significant degree of control over the shape of the shock front has been experimentally demonstrated,¹⁷ such control may not be achievable in many cases. In addition to deviations from perfect planarity of the shock front, the presence of crystal defects can result in variations of the local phase of the polarization current on the shock front surface. To study the role of random imperfections, we consider a model of the shock front that incorporates random fluctuations in phase of the polarization current on the shock front. The minimum spatial wavelength of the phase fluctuations is limited ($2\pi/k_{\text{max}}$) and loosely corresponds to the distance between crystal defects or minimum wavelength of fluctuations in the shock front surface due to nonplanar drive mechanisms, etc.

The integral in Eq. (6) can be written in terms of the Fourier transform of j as $|\int_{\text{shock}} d\vec{r}' j(\vec{r}') e^{-i\omega(|\vec{r}-\vec{r}'|/c)}|^2 = |\tilde{j}(k_x = \frac{\omega}{c} \sin \theta, k_y=0)|^2$ when \vec{r} lies in the x - z plane. Consider the

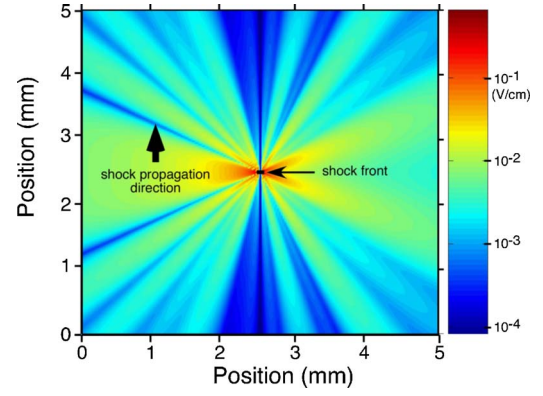


FIG. 13. (Color online) Electric-field magnitude at 22 THz from a $100 \times 100 \mu\text{m}^2$ square shock front for $j_0=0.18 \text{ C/m s}$ for the 22 THz peak on the right side of Fig. 3 and a shock front with random spatial fluctuations in the phase of the polarization current with $k_{\text{max}}=2\pi/(5 \mu\text{m})$. The radiation is not directed but has nodes in the direction of shock propagation.

case where the current $j(\vec{r}')$ possesses spatial fluctuations with wave vectors less than a specified maximum, k_{max} , i.e., let $\tilde{j}(\vec{k}) = \frac{\pi^2}{k_{\text{max}}^2} \sum_{\vec{r}'} j_0 e^{i(\omega/v_s)z(\vec{r}')} e^{-i\vec{k}\vec{r}'}$, where $\vec{r}' = (m \frac{\pi}{k_{\text{max}}}, n \frac{\pi}{k_{\text{max}}})$, where m and n are integers such that $0 \leq m, n < \frac{\sqrt{A} k_{\text{max}}}{\pi}$ for a square shock front and $\frac{\omega}{c} \sin(\theta) \leq k_{\text{max}}$. Here, A is the shock front area. Random fluctuations in $j(\vec{r}')$ can be considered by taking $\frac{\omega}{v_s} z(\vec{r}')$ to be a random variable with value between 0 and 2π for each value of \vec{r}' .

Figure 13 shows the electric-field magnitude at 22 THz from a $100 \times 100 \mu\text{m}^2$ square shock front for $j_0=0.18 \text{ C/m s}$ for the 22 THz peak on the right side of Fig. 3 and a shock front with random spatial fluctuations with $k_{\text{max}}=2\pi/5 \mu\text{m}^{-1}$. The radiation is not directed but has nodes in the direction of shock propagation. The magnitude of the fields is comparable to the case of a curved shock front shown in Fig. 11.

Figure 14 shows the angular dependence of the electric-field magnitude at 22 THz, 1 mm away from a $100 \times 100 \mu\text{m}^2$ square shock front for $j_0=0.18 \text{ C/m s}$ for the 22 THz peak on the right side of Fig. 3. Random spatial variations in the phase of the polarization current are considered with various values of k_{max} . As the deviation from planarity of the shock becomes more pronounced ($2\pi/k_{\text{max}}$ decreases), the emission field amplitudes decrease. The emission in all cases has nodes at $\theta=0$ and $\theta=\pi$ which point in the shock propagation direction and opposite to it, respectively.

An analytical expression for the electric-field expectation can be obtained in the case of random-phase variations in the polarization current. The electric-field expectation is

$$\langle |E(\vec{r})|^2 \rangle = \left[\frac{\mu_0 \omega \sin(\theta)}{4 |r|} \right]^2 \frac{A}{k_{\text{max}}^2} |j_0|^2, \quad (10)$$

which has a distribution similar to that of an oscillating dipole with polarization normal to the shock front. The corresponding power radiated in all directions is given by

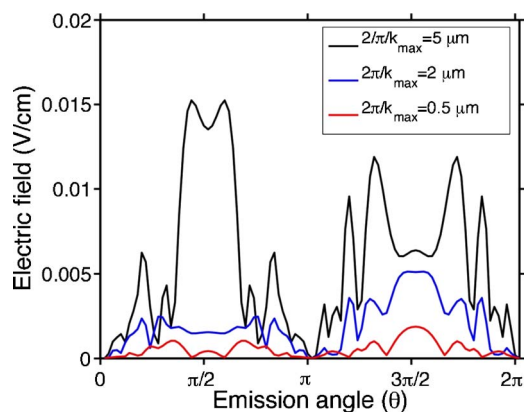


FIG. 14. (Color online) Angular dependence of the electric-field magnitude 1 mm away from a $100 \times 100 \mu\text{m}^2$ square shock front for $j_0 = 0.18 \text{ C/m s}$ for the 22 THz peak on the right side of Fig. 3. Random spatial variations in the phase of the polarization current are considered with various values of k_{max} . As the deviation from planarity of the shock becomes more pronounced (i.e., $2\pi/k_{\text{max}}$ decreases), the emission field amplitudes decrease.

$$\langle p(\omega) \rangle = \frac{\pi \mu_0 \omega^2}{12c} \frac{A}{k_{\text{max}}^2} |j_0|^2. \quad (11)$$

In the case of the 22 THz peak in the right side of Fig. 3 where $j_0 = 0.18 \text{ C/m s}$, for shock front area $A = 1 \text{ cm}^2$ and $2\pi/k_{\text{max}} = 5 \times 10^{-6} \text{ m}^{-1}$, Eq. (11) predicts that the shock coherently radiates with a power of $4 \times 10^{-5} \text{ W}$ while it propagates.

The random shock front case is a worst case scenario: if systems with $k_{\text{max}} \ll \frac{\omega}{c}$ can be achieved (plausible given current state of the art), then the emission can be directed as in Fig. 12, focused, and can have substantially higher emission power that scales with A^2 .

VI. DISCUSSION

Experimental observation of the effect predicted in this work is anticipated to contain several key challenges. Shock waves of a sufficient degree of planarity are most easily generated by laser-drive techniques. Obtaining the necessary small tilt angles (on the order of v_s/c in radians) may be challenging using gun-driven projectile approaches. Large industries revolve around the growth of thin films of high-purity single crystals. Point defects are less likely to be problematic than line or other higher dimensional defects because they are less disruptive of the long-range crystalline order. Thin films of artificial crystals or nanostructures can be grown with precisely designed nanometer length scale lattice constants. Such structures are commonly grown for electronic devices and could be tailored to emit at a desired wavelength.

One of the biggest challenges to experimental observation of the effect discussed in this paper is likely to be detecting the relatively weak signals with existing technology. Detectors in this frequency regime are inefficient compared with optical techniques but are developing rapidly.¹⁸ As discussed in Sec. V, the signal amplitude can vary widely depending on

the details of the experiment. Such amplitudes may be detectable at frequencies above 10 THz using current nonlinear optical techniques that are commonly employed for THz detection. Much more sensitive THz photon counting techniques are being developed.¹⁹ THz generation and detection in general is currently an area of active research.¹⁸ Uses for terahertz radiation range from fundamental studies of phonon dynamics to new methods of medical and biological imaging to security screening devices able to penetrate clothing to detect explosives or other weapons.^{20,21}

Experimental observation of the signal would establish a new lower bound on the rise-time of elastic shock waves in crystals. To our knowledge, the fastest rise-time measurement to date for a shock or soliton-type wave in a material is in excess of about 1 ps.⁴ Observation of a signal above 10 THz from the shock would establish the elastic shock front thickness as a few atomic planes.

When shocked to sufficiently large pressures, crystalline solids undergo irreversible (plastic) deformation of the crystalline lattice. This deformation can be characterized by a wide variety of mechanisms including motion of existing dislocations, creation and motion of new dislocations, shear banding, phase transformations, etc. The perfect crystals of our simulations appear not to undergo irreversible deformation until piston speeds above 1 km/s. There is experimental evidence that plastic deformation can occur as low as 0.02 GPa in NaCl shocked in the [100] direction and as low as 0.8 GPa when shocked in the [111] direction,²² below the 2 GPa stresses of the 200 m/s piston speed simulations. These experiments and our calculations have several key distinctions that may give rise to differing behavior. Our simulations are of perfect crystals in which the energy barrier to plastic deformation is higher than when defects already exist in the material. There is also a significant time scale difference between the experimental observations (0.1 μs time scale) and the simulations (10 ps time scale). Experiments on short time scales indicate that elastically compressed states of silicon can exist at higher pressures than observed on longer time scales.²³

To study the possible role of plastic deformation of the crystal, we have performed a shock simulation with 1 km/s piston speed for a shock propagating in the [100] direction in a 300 K crystal with a small number of atoms removed to form a void. Plastic deformation occurs around the void well behind the shock front and does not effect the shock front on the time scale of the simulation (about 30 ps). The coherent current at 22 THz is still observed. While it is possible that plastic deformation of the crystalline lattice can affect the coherent emission, our simulations show that there is a regime of shock amplitude which is strong enough to observe the effect but weak enough to preclude plastic deformation from affecting the shock front (where the signal is generated) for a period of time.

Since the amplitude of the coherent effect is related to an inherently nonlinear effect at the shock front, it may be expected that the amplitude observed in molecular dynamics simulations is sensitive to nonlinear properties of the empirical interatomic potentials employed. Like most empirical interatomic potentials, the potentials employed in this work are not explicitly fitted to nonlinear material properties. While

this is a common approximation in molecular dynamics simulations with empirical interatomic potentials, it could represent a source of error in the calculated amplitude of the coherent effect. However, it cannot affect the conclusion that coherent radiation can be generated.

Other examples of techniques of radiation generation exist that are based on the general principle of a nonlinear excitation propagating through a periodic medium. One such technique involves sending an ultrafast optical pulse through a periodically poled LiNbO₃ nonlinear optical crystal to generate THz radiation.²⁴ A more closely related technique is the generation of electromagnetic shock waves in periodic nonlinear transmission lines to generate rf radiation.^{25–27}

The generation of phonon polaritons via impulsive stimulated Raman scattering can be used to create many-cycle THz radiation.³ One of the fundamental distinctions of the mechanism presented in this work is that the frequencies generated are not those of harmonic optical or other phonons, i.e., Eq. (3) does not generally correspond to phonon frequencies. In the case of NaCl, nonlinear behavior at the shock front and the periodicity of the crystalline lattice are responsible for generating the frequency components around 16 THz and above that are much higher than the highest linear phonon frequencies of around 10 THz. THz radiation is commonly generated by sending a subpicosecond optical pulse through a material with a second-order nonlinear optical response (optical rectification). The shock wave mechanism can be observed in materials without a second-order nonlinear optical response such as NaCl.

It is useful to consider what happens to the amplitude and frequency of the coherent polarization current in the limit where the shock speed decreases to the longitudinal sound speed, i.e., the limit where the nonlinear mechanical wave becomes linear. In this limit, the possible polarization frequency components of Eq. (3) become

$$\omega = 2\pi\ell \frac{c_l}{a}, \quad (12)$$

where c_l is the longitudinal sound speed in the propagation direction. These frequencies do not correspond with optically active phonon frequencies of the material except in a pathological case where the phonon spectrum is dispersionless. The frequencies of Eq. (12) might be expected to coincide with phonon frequencies in this limit if the effects were a nonlinear form of optically active phonon excitation. As an additional consequence of the shock speed decreasing to the longitudinal sound speed, the rise distance of the shock front becomes large, much larger than a few lattice constants of the crystal. Shock front broadening causes the amplitude of the coherent polarization current to diminish to zero as the shock decreases in amplitude to become a linear wave.⁷

A further theoretical distinction between phonon (resonant) oscillations and the shock-induced nonresonant polarization oscillations of this work is the fundamental limit of the coherence time for radiation produced for these two mechanisms. In the case of an excited optically active phonon, the coherence time is limited by the lifetime of the phonon. In the shock case, the coherence time is limited by the steadiness of the shock and the constancy of the lattice

spacing. In principle, the coherence time of the shock-induced radiation can be made arbitrarily long if a steady shock can be made to propagate arbitrarily far through a crystal with no strain gradients.

It is well known that coherent radiation at almost any frequency can be obtained from a *coherent* source using materials with a nonlinear optical response. Such an approach utilizes radiation from a coherent source to generate new coherent radiation, e.g., frequency tripling of a continuous-wave laser. The coherent radiation mechanism presented in this work is fundamentally distinct from such nonlinear approaches because temporal coherence of the emitted radiation results from the spatial coherence of the crystal lattice rather than another coherent source. The optical nonlinearity mechanism (e.g., 3ω frequency tripling) works in amorphous materials while the shocked crystal mechanism does not. However, the coherence of the signal produced by the shock can depend in some ways on some coherence properties of the source driving the shock wave. The spatial coherence properties of the THz signal are related to the spatial coherence of the source driving the shock and the spatial coherence of the crystal. The temporal history of the source driving the shock can also have an effect on the constancy of the shock speed. For example, if the source driving the shock stops driving, the shock speed will gradually decrease, resulting in a signal chirped in frequency.

It is not necessary for the source generating the shock to contain the high-frequency THz components that are eventually observed when the steady-state shock profile is achieved. The nonlinear behavior of the lattice causes a wave with low-frequency components to steepen up and exhibit higher-frequency components. This mechanism provides a degree of independence from the temporal behavior of the source generating the shock in this case. The simulations of this work utilize an instantaneous acceleration of the piston to a specified piston speed. This gives this shock front a sharp rise from the start of the simulation. We have also performed a [100] direction shock simulation in which the piston is accelerated to 200 m/s over a time period of 1 ps. The generated wave front steepens over a time scale of 10–20 ps after which the 22 THz signal is observed.

VII. CONCLUSION

We have presented molecular dynamics simulations and some analysis showing that coherent polarization currents can be generated when a shock wave propagates through a polarizable crystal. We have shown how these coherent polarization currents can potentially lead to the emission of coherent radiation if the shock front is sufficiently planar. While experimental observation of the signal is likely to be challenging, it is within or nearly within existing experimental capabilities. We believe that this mechanism for generating coherent optical radiation is fundamentally distinct from other sources of coherent optical radiation.

ACKNOWLEDGMENTS

We thank E. Ippen, F. Kaertner, and K. Nelson of MIT, J.

Glownia, A. Taylor, and R. Averitt of LANL, M. Armstrong, L. Fried, D. Hicks, and N. Holmes of LLNL, and W. Nellis of Harvard University for helpful discussions. This work was supported in part by the Materials Research Science and Engineering Center program of the National Science Founda-

tion under Grant No. DMR-9400334. This work was performed in part under the auspices of the U.S. Department of Energy by University of California, Lawrence Livermore National Laboratory under Contract No. W-7405-Eng-48 and the LLNL LDRD office.

*Electronic address: reed23@llnl.gov

- ¹E. J. Reed, M. Soljačić, R. Gee, and J. D. Joannopoulos, *Phys. Rev. Lett.* **96**, 013904 (2006).
- ²A. M. Sessler and D. Vaughan, *Am. Sci.* **75**, 34 (1987).
- ³R. M. Koehl and K. A. Nelson, *J. Chem. Phys.* **114**, 1443 (2001).
- ⁴O. L. Muskens, A. V. Akimov, and J. I. Dijkhuis, *Phys. Rev. Lett.* **92**, 035503 (2004).
- ⁵K. T. Gahagan, D. S. Moore, D. J. Funk, R. L. Rabie, S. J. Bue-low, and J. W. Nicholson, *Phys. Rev. Lett.* **85**, 3205 (2000).
- ⁶J. E. Patterson, A. Lagutchev, W. Huang, and D. D. Dlott, *Phys. Rev. Lett.* **94**, 015501 (2005).
- ⁷E. J. Reed, M. Soljacic, and J. D. Joannopoulos, *Phys. Rev. E* (to be published).
- ⁸G. E. Hauver, *J. Appl. Phys.* **36**, 2113 (1965).
- ⁹R. K. Linde, W. J. Muri, and D. G. Doran, *J. Appl. Phys.* **37**, 2527 (1966).
- ¹⁰P. Harris and H. Presles, *J. Chem. Phys.* **77**, 5157 (1982).
- ¹¹A. Strachan, A. van Duin, D. Chakraborty, S. Dasgupta, and William A. Goddard III, *Phys. Rev. Lett.* **91**, 098301 (2003).
- ¹²E. M. Bringa, J. U. Cazamias, P. Erhart, J. Stolken, N. Tanushev, B. D. Wirth, R. E. Rudd, and M. J. Caturla, *J. Appl. Phys.* **96**, 3793 (2004).
- ¹³S. J. Plimpton, *J. Comput. Phys.* **117**, 1 (1995).
- ¹⁴D. H. Robertson, D. W. Brenner, and C. T. White, *Phys. Rev. Lett.* **67**, 3132 (1991).
- ¹⁵E. Zaretsky, *J. Appl. Phys.* **93**, 2496 (2003).
- ¹⁶C. W. M. Castleton, A. Hoglund, and S. Mirbt, *Phys. Rev. B* **73**, 035215 (2006).
- ¹⁷D. S. Moore, K. T. Gahagan, J. H. Reho, D. J. Funk, S. J. Bue-low, and R. L. Rabie, *Appl. Phys. Lett.* **78**, 40 (2001).
- ¹⁸P. H. Siegel, *IEEE Trans. Microwave Theory Tech.* **50**, 910 (2002).
- ¹⁹S. Komiyama, O. Astafiev, V. Antonov, T. Kutsuwa, and H. Hirai, *Nature (London)* **403**, 405 (2000).
- ²⁰P. H. Siegel and R. J. Dengler, *Proc. SPIE* **5354**, 1 (2004).
- ²¹M. C. Kemp, P. F. Taday, B. E. Cole, J. A. Cluff, A. J. Fitzgerald, and W. R. Tribe, *Proc. SPIE* **5070**, 44 (2003).
- ²²W. J. Murri and G. D. Anderson, *J. Appl. Phys.* **41**, 3521 (1970).
- ²³A. Loveridge-Smith, A. Allen, J. Belak, T. Boehly, A. Hauer, B. Holian, D. Kalantar, G. Kyrala, R. W. Lee, P. Lomdahl, M. A. Meyers, D. Paisley, S. Pollaine, B. Remington, D. C. Swift, S. Weber, and J. S. Wark, *Phys. Rev. Lett.* **86**, 2349 (2001).
- ²⁴Y. S. Lee, T. Meade, V. Perlin, H. Winful, and T. B. Norris, *Appl. Phys. Lett.* **76**, 2505 (2000).
- ²⁵A. M. Belyantsev and S. L. Klimin, *Izv. Vyssh. Uchebn. Zaved., Radiofiz.* **36**, 1011 (1993).
- ²⁶A. M. Belyantsev, A. I. Dubnev, S. L. Klimin, Y. A. Kobelev, and L. A. Ostrovskii, *Tech. Phys.* **40**, 820 (1995).
- ²⁷N. Seddon and T. Bearpark, *Science* **302**, 1537 (2003).